*sustainability*

MDPI

*Article*

# Insights into Microscopic Characteristics of Gasoline and Ethanol Spray from a GDI Injector Under Injection Pressure up to 50 MPa

**Xiang Li [1,2,*], Xuewen Zhang [1], Tianya Zhang [1], Ce Ji [1], Peiyong Ni [1], Wanzhong Li [2,*], Yiqiang Pei [2,*], Zhijun Peng [3] and Raouf Mobasheri [4]**

[1] School of Mechanical Engineering, Nantong University, Nantong 226019, China; zhangxuewen@ntu.edu.cn (X.Z.); 2310110325@stmail.ntu.edu.cn (T.Z.); jice@stmail.ntu.edu.cn (C.J.); nipeiyong@ntu.edu.cn (P.N.)
[2] State Key Laboratory of Engines, Tianjin University, Tianjin 300072, China
[3] School of Engineering, University of Lincoln, Lincoln LN6 7DQ, UK; jpeng@lincoln.ac.uk
[4] ICL, Junia, Université Catholique de Lille, LITL, F-59000 Lille, France; raouf.mobasheri@junia.com
* Correspondence: xiang.li@ntu.edu.cn (X.L.); lwzhong@tju.edu.cn (W.L.); peiyq@tju.edu.cn (Y.P.)

**Abstract:** Nowadays it has become particularly valuable to control the Particulate Matter (PM) emissions from the road transport sector, especially in vehicle powertrains with an Internal Combustion Engine (ICE). However, almost no publication has focused on a comparison of the microscopic characteristics of gasoline and ethanol spray under injection pressure conditions of more than 30 MPa, except in the impingement process. By using a Phase Doppler Particles Analyser (PDPA) system, the microscopic characteristics of gasoline and ethanol spray from a Gasoline Direct Injection (GDI) injector under injection pressure ($P_I$) up to 50 MPa was fully explored in this research. The experimental results demonstrate that under the same $P_I$, the second peak of the probability ($p_d$) curves of droplet normal velocity for gasoline is slightly higher than that of ethanol. Moreover, gasoline spray exceeds ethanol by about 5.4% regarding the average droplet tangential velocity at 50 mm of jet downstream. Compared to ethanol, the $p_d$ curve's peak of droplet diameter at (0, 50) for gasoline is 1.3 percentage points higher on average, and the overall Sauter mean diameter of gasoline spray is slightly smaller. By increasing $P_I$ from 10 MPa to 50 MPa, $p_d$ of the regions of "100 $\leq$ Weber number ($We$) < 1000" and "$We \geq 1000$" increases by about 23%, and the $p_d$ of large droplets over 20 µm shows a significant reduction. This research would provide novel insights into the deeper understanding of the comparison between gasoline and ethanol spray in microscopic characteristics under ultra-high $P_I$. Additionally, this research would help provide a theoretical framework and practical strategies to reduce PM emissions from passenger vehicles, which would significantly contribute to the protection and sustainability of the environment.

**Keywords:** microscopic spray characteristics; high injection pressure; gasoline; ethanol; Gasoline Direct Injection (GDI) injector; Phase Doppler Particles Analyser (PDPA)

check for updates

**Citation:** Li, X.; Zhang, X.; Zhang, T.; Ji, C.; Ni, P.; Li, W.; Pei, Y.; Peng, Z.; Mobasheri, R. Insights into Microscopic Characteristics of Gasoline and Ethanol Spray from a GDI Injector Under Injection Pressure up to 50 MPa. *Sustainability* **2024**, *16*, 9471. https://doi.org/10.3390/su16219471

Academic Editor: Janusz Kozinski

Received: 26 September 2024
Revised: 20 October 2024
Accepted: 28 October 2024
Published: 31 October 2024

**Copyright:** © 2024 by the authors. Licensee MDPI, Basel, Switzerland. This article is an open access article distributed under the terms and conditions of the Creative Commons Attribution (CC BY) license (https://creativecommons.org/licenses/by/4.0/).

## 1. Introduction

In recent decades, air quality has been a major concern related to environmental protection, sustainable development, and human health in many countries [1–4]. The level of Particulate Matter (PM) emissions from road transport can profoundly affect air quality [5,6]. Moreover, stricter PM emission standards have been imposed on passenger vehicles and other types of road-based transportation [3]. Therefore, in order to minimise PM emissions efficiently, reliably, and economically, a variety of efforts have been made to develop vehicle powertrain systems, which can be classified into two categories based on whether Internal Combustion Engines (ICEs) are being utilised.

Regarding vehicle powertrains without ICEs, the most popular type is battery electric, which relies solely on power from the chemical energy offered by rechargeable battery

packs [7]. The greatest advantage of Battery Electric Vehicles (BEVs) for environmental protection is that no tail emissions can be produced during the operation. However, the promotion and practicability of BEVs is severely limited by the long recharging time and the construction of relevant infrastructure [8,9]. Additionally, the pollution from power stations should not be overlooked if the electricity is generated from fossil fuels, especially coal and oil [10,11].

The other typical powertrain without an ICE is fuel cell, which normally generates electricity by converting chemical energy from hydrogen and oxygen [12–15]. As an innovative technology to achieve zero harmful tail emissions, a highly competitive benefit of Fuel Cell Electric Vehicles (FCEVs) is that its refuelling time is similar to conventional ICE vehicles, which is far less than the recharging time of BEVs [16]; whereas the high initial cost for consumers and very limited infrastructure of hydrogen refuelling stations adversely impacts the development popularity of FCEVs [17].

Regarding vehicle powertrains with ICEs, two promising alternative fuels are hydrogen and ammonia, primarily due to the advantage of carbon-free components [18–20]. Hydrogen ICEs mainly face the challenges of abnormal combustion conditions, such as pre-ignition, backfire, and knock [19,21]. For the application of ammonia ICEs, it mainly has practical difficulties in improving combustion efficiency, owing to the ammonia characteristics of high ignition energy, narrow flammability range, low reaction rate, slow flame propagation, and low flame temperature [22–24]. The Oxy-Fuel Combustion (OFC) concept with carbon capture provides another way to control the harmful emissions from vehicles [25–27]. However, limited by its practicability, complexity, and high cost, the application of OFC on vehicles is generally in the early research stage [28–31].

Therefore, it is still an important issue to minimise PM emissions from Hybrid Electric Vehicles (HEVs) and conventional ICE-only vehicles, which are expected to remain of the most common power resources for road transport for a long time [32–34]. Direct Injection (DI) systems, such as Gasoline Direct Injection (GDI) or dual-injection, have become predominant technologies in Spark Ignition (SI) engines due to the performance improvements in thermal efficiency, knock resistance, and transient response [35–39]. Moreover, some researchers have focused on the effects of high fuel injection pressure in no less than 30 MPa of a GDI injector on engine performance and spray characteristics.

Lee et al. [40] demonstrated that as the injection pressure for n-heptane spray increases from 20 MPa to 30 MPa, the occurrence of a branch-like structure can be advanced, but the reduction of droplet size is not significant. Similarly, Medina et al. [41] found that in comparison to the increase from 10 MPa to 20 MPa, the advantage in decreasing particulate numbers becomes weaker with the increase from 20 MPa to 30 MPa. Hoffmann et al. [42] concluded that both the particulate number and mass can be greatly reduced by increasing injection pressure from 5 MPa to 40 MPa in a single-cylinder GDI engine fueled with gasoline. In the meantime, it was observed that fuel consumption can be decreased by around 2%. Park et al. [43] demonstrated that there is a reduction of 10.3% in engine total hydrocarbon emissions when increasing injection pressure from 10 MPa to 50 MPa in a single-cylinder GDI engine fueled with gasoline. Moreover, a great benefit can be derived in mitigating PM emissions from this engine fueled with an ethanol–gasoline blended fuel [44]. By utilising a high-speed schlieren imaging system, Li et al. [45] compared and analysed the macroscopic characteristics between gasoline and ethanol spray of a GDI injector on the front and side views under a 60 MPa injection pressure. Li et al. [46] also systematically assessed the development and characteristics of gasoline and ethanol spray after impingement under 50 MPa injection pressure. Luo et al. [47] investigated the microscopic characteristics of 30 MPa n-heptane near-nozzle spray at both the initial and final stages using the technology of particle image analysis. A statistical analysis was also conducted to study the impacts of cross-flow on iso-octane spray characteristics under injection pressure up to 35 MPa [48].

Regarding engines with a DI system, previous research demonstrated that increasing injection pressure could effectively reduce the PM emissions. Some important progress has

also been made regarding the spray macroscopic and microscopic characteristics under high injection pressure conditions, especially for gasoline and n-heptane. However, under injection pressure conditions of more than 30 MPa, very little research focused on the microscopic characteristics of ethanol spray from GDI injector, and almost no articles have been published that clearly present a comparison of the microscopic characteristics between gasoline and ethanol spray, except in the impingement process. Moreover, this exploration and comparison would be highly valuable because ethanol is one of the most consumed alternative fuels, which contributes a lot to reducing PM emissions and carbon neutrality [49–52].

In this research, an experiment was conducted to quantitatively compare various parameters related to the velocity and size of spray droplets between gasoline and ethanol spray under injection pressure up to 50 MPa. The findings will help gain a comprehensive understanding of microscopic spray characteristics from GDI injectors under ultra-high injection pressure. Furthermore, these novel insights will aid in developing a theoretical foundation and practical solution for mitigating PM emissions from GDI or dual-injection engines fuelled with gasoline and ethanol, thereby meeting stringent automotive emissions regulations and significantly promoting environmental sustainability.

## 2. Experimental Methodology

### *2.1. Experimental Setup and Procedure*

As shown in Figure 1, a Phase Doppler Particles Analyser (PDPA) test system was set up to achieve instantaneous and precise measurements of microscopic spray characteristics. The main components of the system are an argon–ion laser, a beam separator, a transmitter, and a receiver. Due to being mounted on a removable three-dimensional coordinate frame, a high-precision movement with a 0.1 mm step size for the transmitter and receiver can be realised to locate test points. Besides, a signal processor with an ultra-high sampling frequency of up to 180 MHz could fully meet the real-time measurement requirements for high-speed spray droplets. During this test, the laser power was configured at 1.3 W, and the laser wavelength ranged from 488 nm to 514.5 nm. The setup for measuring droplet velocity spanned from −151.95 m/s to 238.77 m/s, while measuring droplet diameter can be from 0 μm to 236 μm with a 0.1 μm resolution. It should also be noted that the PDPA system is able to detect the velocity and diameter of particles that are nearly spherical in shape, and therefore, deformed or non-spherical droplets are not within the measuring range.

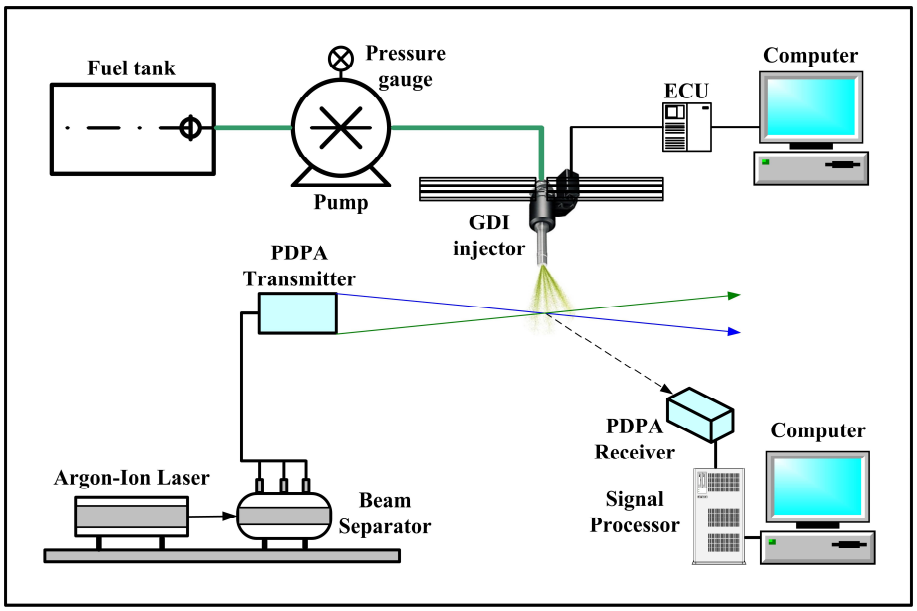



**Figure 1.** A schematic diagram of the experimental setup.

The two fuels employed in this test are gasoline and ethanol, which are outlined in Table 1 [53]. The GDI injector employed in this research is a five-nozzle injector with a 0.174 mm inner diameter, normally used in advanced dual-injection SI engines. The injector was secured on a custom-fabricated metal stand before the test, ensuring stabilisation during the test.

**Table 1.** The fuel properties of gasoline and ethanol [53].

| Fuel Type | Gasoline | Ethanol |
|---|---|---|
| Chemical formula | C5–C12 | $C_2H_5OH$ |
| Relative molecular mass | 95–120 | 46 |
| Gravimetric oxygen content (%) | <1 | 34.78 |
| Research octane number | 95 | 107 |
| Density (293 K) (kg/L) | 0.73 | 0.789 |
| Vapour density (293 K) (kg/m$^3$) | 3.88 | 2.06 |
| Kinematic viscosity (293 K) (mm$^2$/s) | 0.71 | 1.52 |
| Surface tension coefficient (293 K) (mN/m) | 22 | 21.97 |
| Boiling range (K) | 303–473 | 351 |
| Low heating value (kJ/kg) | 44,300 | 26,900 |
| Latent heat of vaporisation (kJ/kg) | 370 | 840 |
| Laminar flame speed (293 K) (m/s) | 0.33 | 0.5 |
| Stoichiometric air–fuel ratio | 14.7 | 8.95 |

Figure 2 illustrates the injector's nozzle geometry and the PDPA test points. A coordinate system was introduced to visually represent the spatial positions of these test points. The positive direction of "X-axis" and "Y-axis" corresponds to rightward and downward, respectively. For instance, point (8, 50) is 8 mm to the right and 50 mm below the nozzle, while (−12, 50) is 12 mm to the left and 50 mm below. Most test points were selected on the plane of 50 mm downstream directly below the injector according to the Society of Automotive Engineers (SAE) J2715 recommended practice [54]. Along this plane, test points were selected at intervals of 4 mm, extending towards the edge of "jet 1". Besides, (0, 60) and (0, 70) are selected to further explore the characteristics of droplet breakup and atomisation along the vertical direction of spray development.

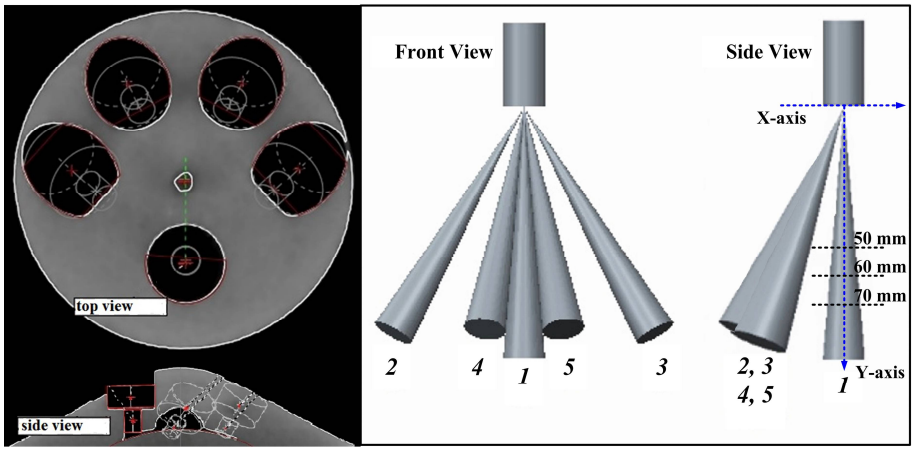



**Figure 2.** The nozzle geometry and PDPA test points.

Moreover, an Electronic Control Unit (ECU) was utilised to synchronise the PDPA data with the fuel injection signal. Using a high-precision pump with a resolution of 0.1 MPa, fuel was injected into an ambient environment. The temperature and pressure of the ambient environment are 293 ± 0.5 K and 0.1 MPa, respectively. The fuel injection pressure in this research ranged from 10 MPa to 50 MPa, representing the conditions of standard to ultra-high pressures. A short pulse of 1.2 ms and a low frequency of 0.1 Hz

was set up for fuel injection to minimise potential interferences by the suspended droplets from the previous injection. To further ensure the reliability of the results, a minimum of 20,000 validated droplets were sampled by multiple fuel injections under each test condition, and this test procedure was repeated three times. Additionally, an air extraction hood was used to eliminate suspended droplets from the testing site, thereby minimising potential safety hazards.

### *2.2. Key Parameters*

In order to provide a more comprehensive analysis of the experimental results, several key parameters have been introduced to this research as follows.

$P_I$ represents fuel injection pressure. $V_N$ and $V_T$ represent the normal component and tangential component of droplet velocity, respectively. As illustrated in Figure 3, the positive direction of $V_N$ is defined as vertically downward, while the positive direction of $V_T$ is horizontally to the right.

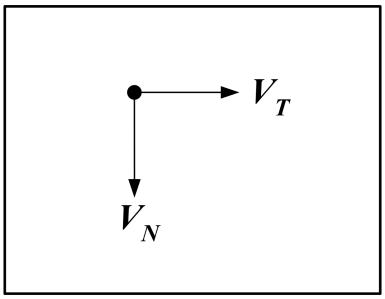



**Figure 3.** The positive directions of $V_N$ and $V_T$.

$t$ represents time after start of fuel injection (ASOI); $p_d$ represents abbreviation of probability; and $D_d$ represents the droplet diameter. As presented in Equation (1), $D_{SMD}$ represents Sauter mean diameter of droplets, which is widely adopted to reflect the atomisation degree.

$$D_{SMD} = \frac{\sum_{i=1}^{N} n_i D_i^3}{\sum_{i=1}^{N} n_i D_i^2} \quad (1)$$

Here, $N$ represents number of droplets, and $n_i$ represents number of droplets with diameter $D_i$.

Within the figures of the next chapter, some abbreviations were used to make the label of spray cases more concise and clear. For example, "10-G" represents gasoline spray under $P_I$ of 10 MPa, and "50-E" represents ethanol spray under $P_I$ of 50 MPa.

## 3. Results and Discussion

### *3.1. Velocity of Spray Droplets*

Figure 4 presents $p_d$ of $V_N$ at (0, 50) under $P_I$ of 10 MPa and 50 MPa. It can be seen that the $p_d$ curves of $V_N$ show different forms between the conditions of $P_I$ = 10 MPa and $P_I$ = 50 MPa. First of all, although the curves show approximate bimodal distribution forms, the highest peak, located at 2 m/s, rises from about 25% to 45% by increasing $P_I$ from 10 MPa to 50 MPa. This is mainly due to the fact that under $P_I$ = 50 MPa, the trend of droplet breakup would be effectively raised, enhancing the irregularity of the droplet trajectory. Hence, a relatively high proportion of suspended droplets with $V_N$ approaching 0 m/s can be observed.

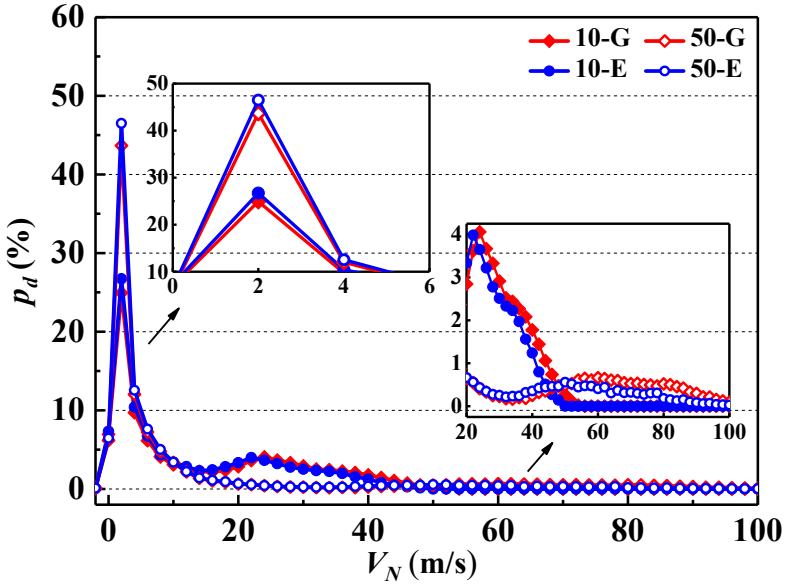



**Figure 4.** $p_d$ of $V_N$ at (0, 50) under $P_I$ of 10 MPa and 50 MPa.

Besides, the curve's second peak for both gasoline and ethanol spray occurs around the $V_N$ of 22 m/s under $P_I$ = 10 MPa, and almost no proportion can be found above 50 m/s. However, under $P_I$ = 50 MPa, a soft peak form occurs at approximately 60 m/s, indicating that ultra-high $P_I$ would promote the production of high $V_N$ droplets, thereby developing the spray penetration. Meanwhile, it shows that compared to ethanol, the second peak of gasoline is slightly higher under the same $P_I$. This can be explained by Bernoulli's principle, as shown in Equation (2). Under equivalent conditions of $P_I$ and height, the fluid density of gasoline is lower than that of ethanol, thus leading to a higher $V_N$.

$$\frac{1}{2}\rho_L v^2 + \rho_L g z + P = C \tag{2}$$

Here, $\rho_L$ and $v$ represent fluid density and fluid speed, respectively. $g$ represents gravitational acceleration; $z$ represents elevation of a point above a reference plane; $P$ represents pressure at the chosen point; and $C$ denotes a constant.

Figure 5 presents the average $V_N$ at (0, 50) as $t$ progresses under different $P_I$. Overall, the variation of $V_N$ shows a similar trend under all the $P_I$ conditions. Initially, the droplets at the spray-leading edge have relatively high average $V_N$ compared to the subsequent droplets, and the maximum value could exceed 60 m/s under $P_I$ = 50 MPa. An apparent reduction can be found in the average $V_N$ as $t$ progresses under all the $P_I$ conditions, and the beginning of the reduction could be advanced from 1.4 ms ASOI to 0.7 ms ASOI by increasing $P_I$ from 10 MPa to 50 MPa. The main reason is that owing to the spray collapse and droplet breakup, the irregularity of the droplet motion could be greatly increased, resulting in a large number of droplets at very low speed. Moreover, the extent of the droplets' breakup and motion irregularity can be further enhanced under ultra-high $P_I$.

In order to fully assess the trend and extent of spray tangential diffusion, Figure 6 illustrates average $V_T$ at 50 mm of jet downstream under different $P_I$. Three main findings can be obtained as follows. First, it is evident that increasing $P_I$ could improve the average $V_T$ for both gasoline and ethanol spray. The absolute value of the maximum average $V_T$ can increase up to around 4 m/s at both (−16, 50) and (16, 50) under $P_I$ = 50 MPa. This is mainly because by increasing $P_I$, the kinetic energy of droplets is enhanced to support more production of some droplets with high $V_T$. Second, relative to the droplets at the axial centre of the jet, $V_T$ of droplets near the edge can be higher due to the impacts of the vortex, and the interaction between adjacent jets. Moreover, owing to the interaction force between jets, the absolute value of $V_T$ at (−16, 50) is relatively high compared to that at (−16, 50). Third, under the same $P_I$, the absolute value of $V_T$ of gasoline is on average 5.4%

higher than that of ethanol, which contributes to the horizontal development of the spray, facilitating a more homogeneous air–fuel mixture.

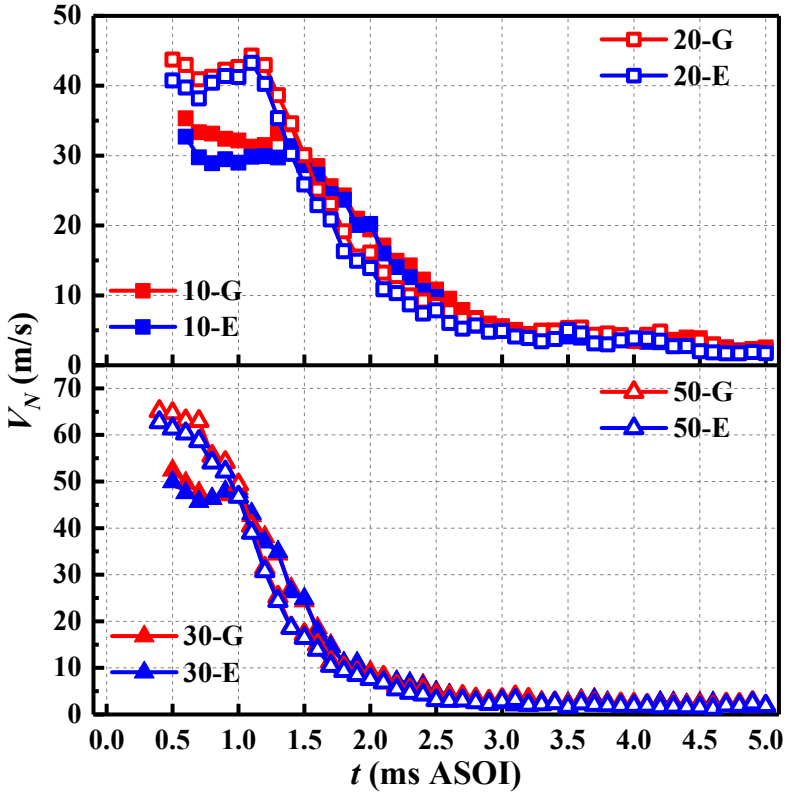



**Figure 5.** The average $V_N$ at (0, 50) as $t$ progresses under different $P_I$.

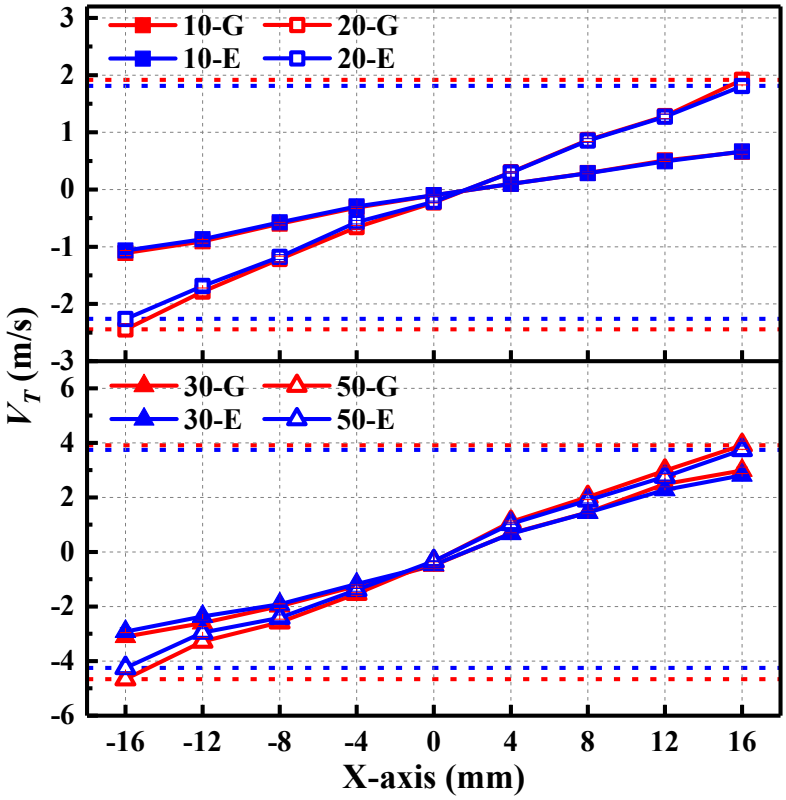



**Figure 6.** The average $V_T$ at 50 mm of jet downstream under different $P_I$.

### 3.2. Size of Spray Droplets

Figure 7 shows $D_{SMD}$ at (0, 50) as $t$ progresses under different $P_I$. It can be found that under all the $P_I$ conditions, $D_{SMD}$ is relatively large when the spray first arrives at (0, 50), followed by a gradual reduction as $t$ progresses. This is affected by the air resistance, and the tendency of collision and coalescence between droplets would increase at the spray-leading edge, thereby forming some droplets with large $D_d$.

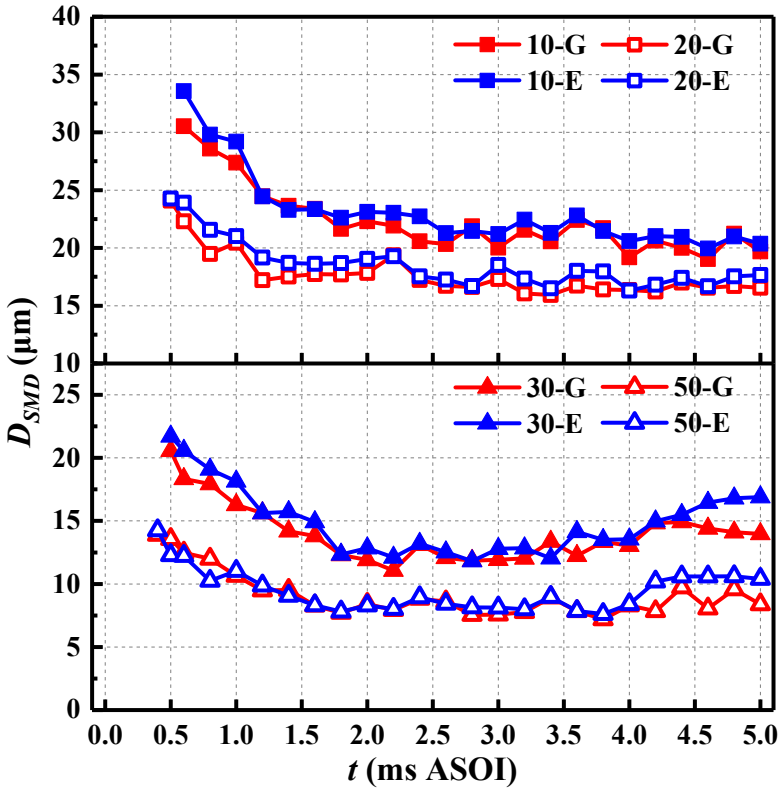



**Figure 7.** $D_{SMD}$ at (0, 50) as $t$ progresses under different $P_I$.

Subsequently, $D_{SMD}$ would become stable within a certain range, which varies depending on the magnitude of $P_I$. Under $P_I$ of 10 MPa and 20 MPa, the stable value of $D_{SMD}$ is around 21 μm and 17 μm, respectively. While the value is reduced to around 13.5 μm and 8.5 μm under $P_I$ of 30 MPa and 50 MPa.

Figures 8 and 9 present $p_d$ of $D_d$ at (0, 50) under $P_I$ of 10 MPa, 20 MPa, 30 MPa, and 50 MPa. It can be seen that with the increase of $P_I$ from 10 MPa to 50 MPa, the location of the curve's peak reduces from 8 μm to 4 μm. Furthermore, the magnitude of the peak rises from 13.3% to 26.9% for gasoline, and it rises from 12.2% to 25.6% for ethanol. Regarding the relatively large droplets of more than 20 μm, $p_d$ exhibits a significant reduction by increasing $P_I$. Particularly, $p_d$ of large droplets is close to 0% for both gasoline and ethanol spray under $P_I$ = 50 MPa, indicating that the secondary atomisation process would be effectively accelerated under ultra-high $P_I$.

This can be explained by the Reynolds number ($Re$) and Weber number ($We$), as shown in Equations (3) and (4). By increasing $P_I$, $V_N$ of droplets that have just come out the of injector nozzle could be increased, leading to a higher $Re$ and $We$. Hence, the intensity of spray vortex and interaction could be enhanced, and more droplets would have a greater potential to break up, reducing the $p_d$ of large droplets. It would help form a more homogeneous mixture, thus further reducing the possibility of PM formation from the in-cylinder of the engine.

$$Re = \frac{V_N D_d}{\nu} \tag{3}$$

$$We = \frac{\rho_L V_N^2 D_d}{\sigma} \quad (4)$$

Here, *Re* represents Reynolds number; *We* represents Weber number; $V_N$ represents normal component of droplet velocity; $v$, $\rho_L$ and $\sigma$ represent kinematic viscosity, density, and surface tension coefficient of the fuel, respectively.

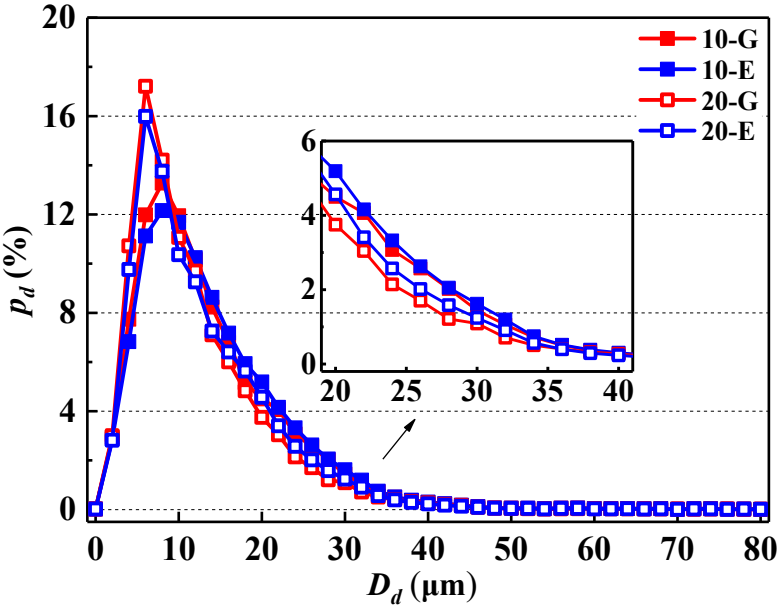



**Figure 8.** $p_d$ of $D_d$ at (0, 50) under $P_I$ of 10 MPa and 20 MPa.

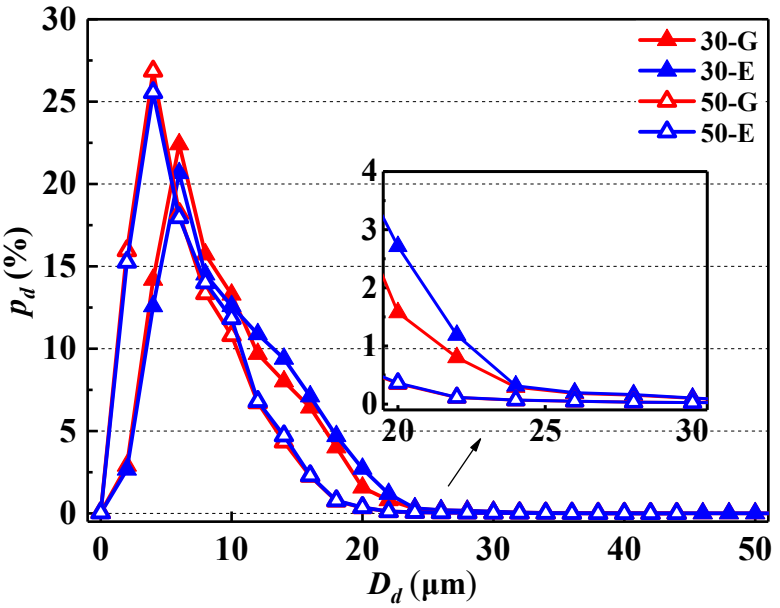



**Figure 9.** $p_d$ of $D_d$ at (0, 50) under $P_I$ of 30 MPa and 50 MPa.

In comparison to ethanol, the $p_d$ curve's peak of gasoline is 1.3 percentage points higher on average under the same $P_I$, indicating that the distribution of $D_d$ slightly moves to the smaller size. As mentioned in the fuel properties of Table 1, compared to ethanol, the kinematic viscosity of gasoline is quite low, while the surface tension coefficient is very close. Therefore, a benefit from smaller $D_d$ and higher $V_N$ is that a higher *We* can be obtained for more droplets of gasoline spray than ethanol using Equation (4). Consequently,

gasoline spray would have a greater potential to break up than ethanol, further leading to tiny droplets.

In order to gain a deeper understanding of the droplet size characteristics, Figure 10 presents $p_d$ of droplets at (0, 50) based on the classification criteria of *We* from Arcoumanis et al. [55,56]. Although, the vibration and bag-like deformation would happen to some droplets with "$We < 100$" on the jet edge, resulting in a process of gradual breakup. These droplets are still comparatively stable compared to the regions of "$100 \leq We < 1000$" and "$We \geq 1000$" [55].

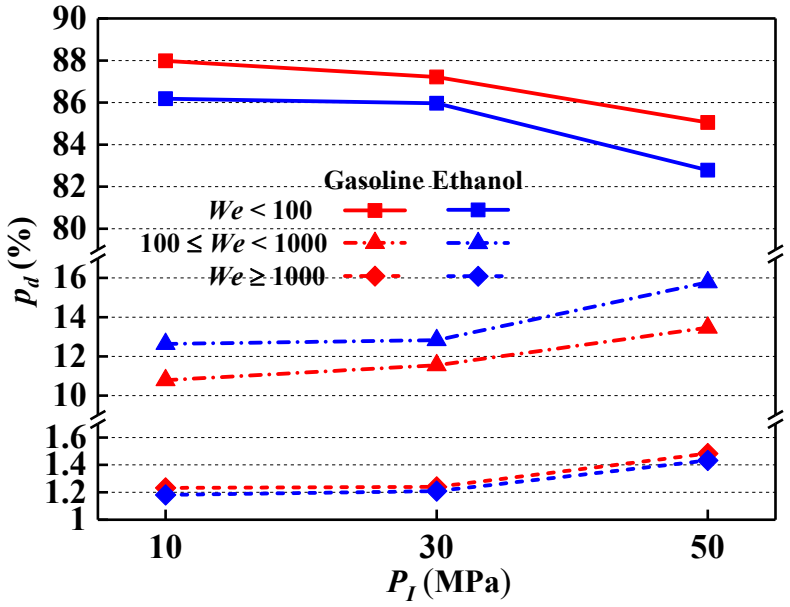



**Figure 10.** $p_d$ of droplets at (0, 50) based on the classification of *We*.

It can be observed that ultra-high $P_I$ contributes to the decreasing of the $p_d$ of relatively stable droplets. By increasing $P_I$ from 10 bar to 50 bar, $p_d$ of "$We < 100$" for the droplets of gasoline and ethanol reduce from 87.9% and 86.2% to 85.1% and 82.8%, respectively. Simultaneously, $p_d$ of the regions of "$100 \leq We < 1000$" and "$We \geq 1000$" show a trend of moderate increase, which are about 1.23 times under $P_I$ = 50 MPa relative to that of $P_I$ = 10 MPa. This indicates that it could contribute to the occurrence of continuous ripping and explosive fragmentation for both gasoline and ethanol spray by implementing $P_I$ of 50 MPa, upgrading the quality of the air–fuel mixture.

Figures 11 and 12 present $D_{SMD}$ at (−16, 50) and (16, 50) as $t$ progresses under different $P_I$. On the whole, it can be seen that for gasoline and ethanol spray as $t$ progresses, $D_{SMD}$ at the two jet edge points of (−16, 50) and (16, 50) exhibit a similar trend to that at (0, 50) of Figure 7. Under all the $P_I$ conditions, $D_{SMD}$ of spray is comparatively large upon reaching the test points. The maximum values of $D_{SMD}$ under $P_I$ of 10 MPa, 20 MPa, 30 MPa and 50 MPa are each around 32 µm, 22.5 µm, 21.5 µm, and 13.5 µm. As $t$ progresses, a decline of more than 5 µm can be found for all the curves, followed by a subsequent decrease towards stabilisation. The stable value of $D_{SMD}$ ranges from around 9 µm under $P_I$ = 50 MPa to around 22 µm under $P_I$ = 10 MPa. Additionally, the overall $D_{SMD}$ of gasoline spray is slightly smaller than that of ethanol under the same $P_I$.

To further study the variations in $D_{SMD}$ of the horizontal positions, Figure 13 presents $D_{SMD}$ at 50 mm of jet downstream under different $P_I$. Three main aspects of findings can be found, as illustrated below.

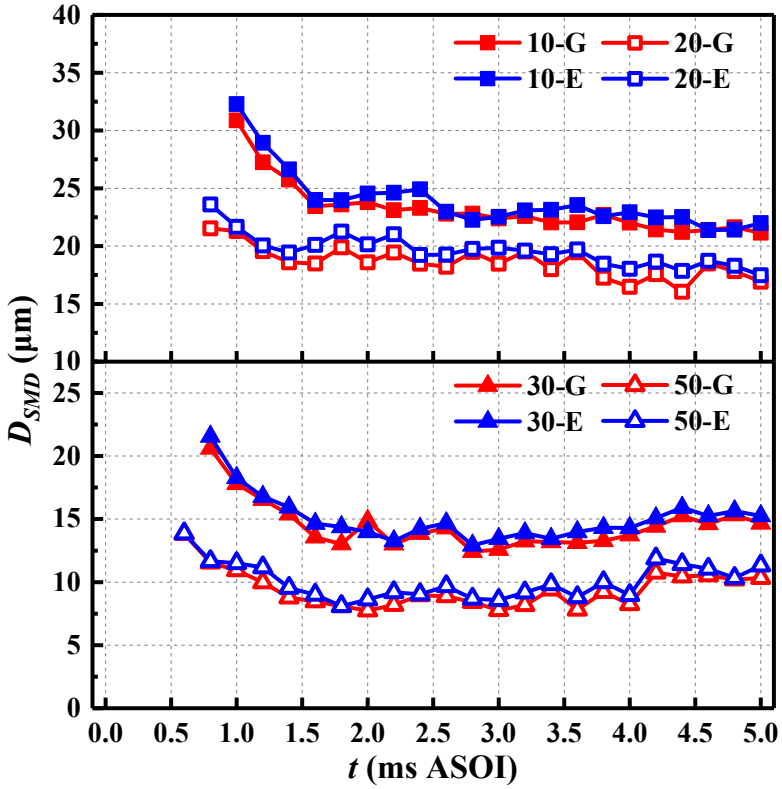



**Figure 11.** $D_{SMD}$ at (−16, 50) as $t$ progresses under different $P_I$.

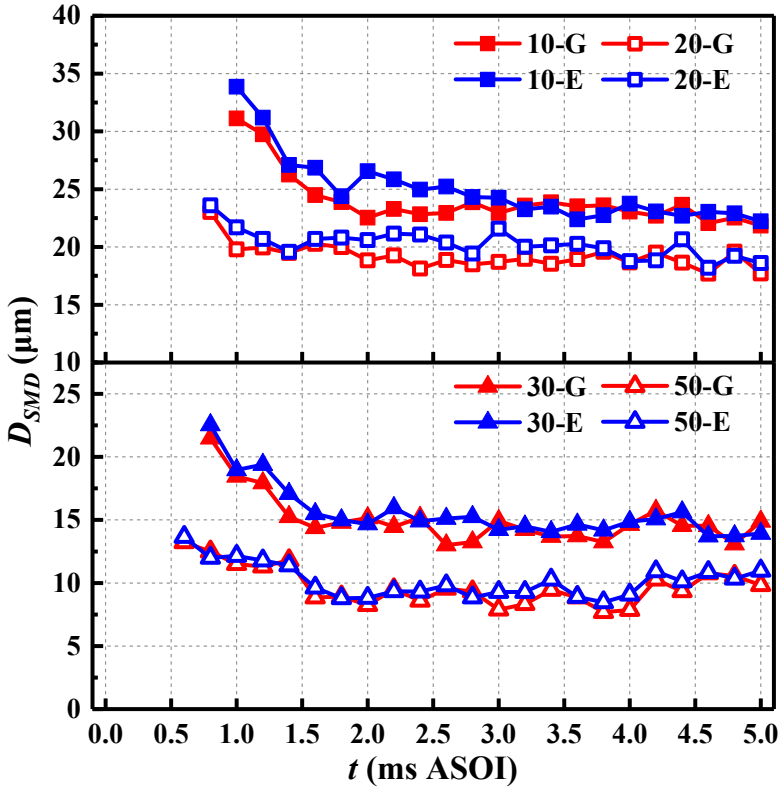



**Figure 12.** $D_{SMD}$ at (16, 50) as $t$ progresses under different $P_I$.

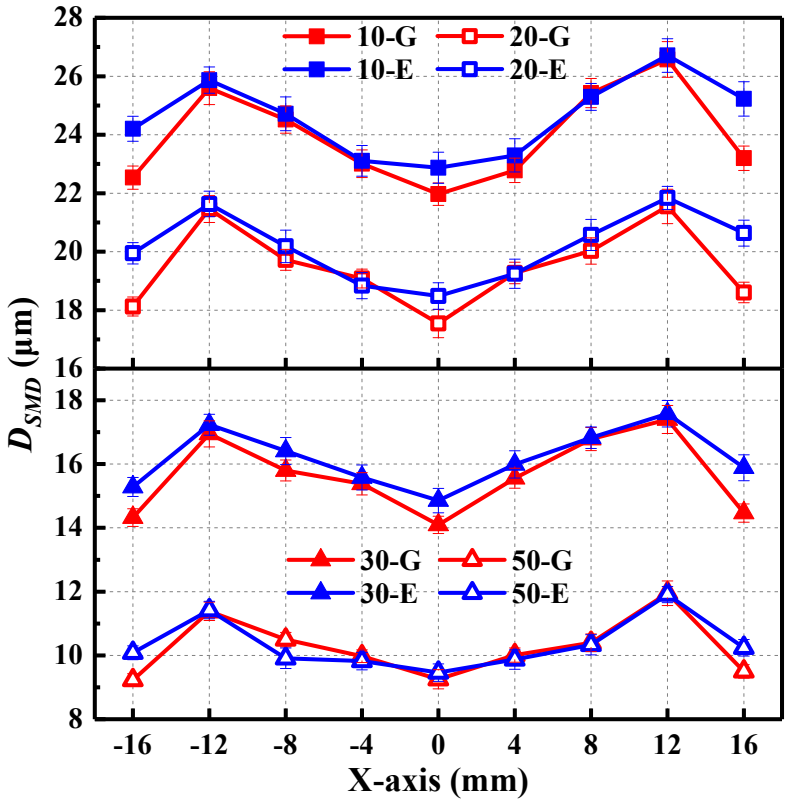



**Figure 13.** $D_{SMD}$ at 50 mm of jet downstream under different $P_I$.

First, it can be found that under the same $P_I$, along the horizontal direction from the axial centre of the jet, $D_{SMD}$ shows a trend of initial enlargement to (−12, 50) or (12, 50), succeeded by a decline on the edge (−16, 50) or (16, 50) under all the $P_I$ conditions. Moreover, in comparison to (16, 50), $D_{SMD}$ at (−16, 50) is approximately 1% to 4% smaller. The variation trend can be mainly attributed to the impacts of air resistance and shear force. Under the influence of air resistance, the occurrence of droplet collision and coalescence becomes more frequent, leading to an increase in $D_d$. Conversely, the shear force and vortices on the outer edge of would accelerate the process of droplet breakup, which leads to the decline in (−16, 50) or (16, 50). Especially, the interaction force between adjacent jets would help further reduce the $D_{SMD}$ at (−16, 50).

Second, compared to ethanol, $D_{SMD}$ of gasoline spray exhibits a relatively sharp decline between (−12, 50) and (−16, 50) or (12, 50) and (16, 50). This is mainly due to higher *We* and vapour density, the breakup, atomisation, and that the evaporation of gasoline spray is faster than those of ethanol, further contributing to the decrease of $D_d$ on the outer edge of the jet.

Third, a significant reduction in $D_{SMD}$ can be obtained at all the test points by increasing $P_I$. For instance, under $P_I$ = 10 bar, the maximum value of $D_{SMD}$ would occur at (12, 50), which are 26.6 μm and 26.7 μm for gasoline and ethanol, respectively. Under $P_I$ of 30 MPa and 50 MPa, the corresponding value reduce to around 17.5 μm and around 11.9 μm.

Figure 14 presents $D_{SMD}$ at (0, 50), (0, 60), and (0, 70) under different $P_I$. Overall, it can be observed that for both gasoline and ethanol, there is a gradually increasing trend in $D_{SMD}$ along the vertical direction of spray development.

At the microscopic level, the magnitude of increase is slightly different between the standard and ultra-high pressures. Under $P_I$ of 10 MPa and 20 MPa, $D_{SMD}$ at (0, 70) is about 2 μm larger than that at (0, 50). However, the corresponding increment can be widened up to 2.9 μm and 3.3 μm under $P_I$ of 30 MPa and 50 MPa, respectively. This is primarily because over a relatively long distance, large $D_d$ would be formed after more frequent collision and coalescence between droplets by the impacts of air resistance of the

spray-leading edge. Furthermore, the magnitude of impacts would be increased under ultra-high $P_I$ due to higher $Re$ and $We$, which widen the gap in $D_{SMD}$ between (0, 70) and (0, 50).

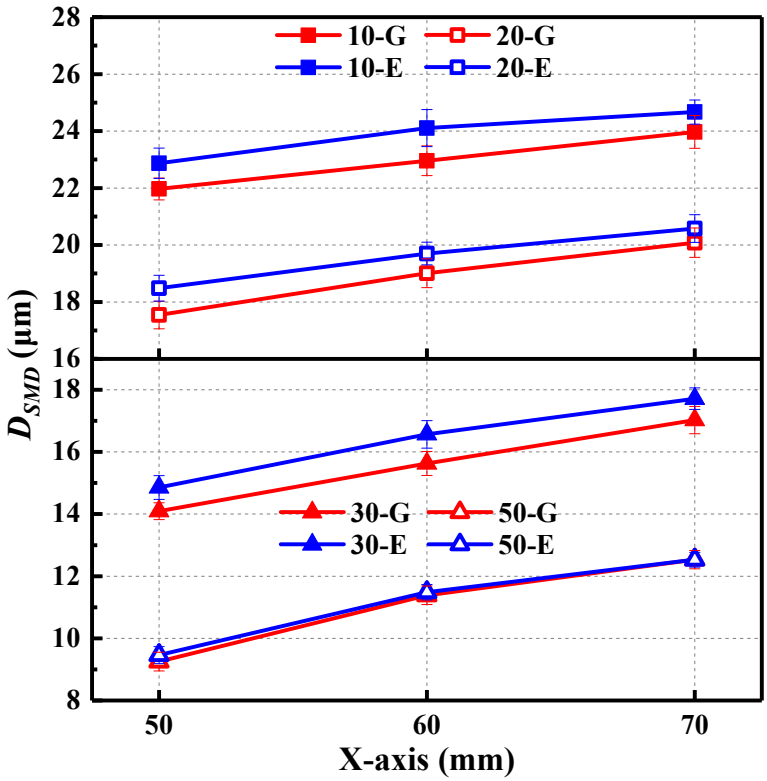



**Figure 14.** $D_{SMD}$ at (0, 50), (0, 60) and (0, 70) under different $P_I$.

## 4. Conclusions

By utilising a PDPA test system and a GDI injector, the microscopic characteristics of gasoline and ethanol spray under $P_I$ up to 50 MPa have been explored in this research. With a statistical analysis, the research findings could provide novel insights into the comparison between gasoline and ethanol spray in the atomisation process and air–fuel mixture quality under ultra-high $P_I$ conditions. The main findings can be concluded as follows.

(1) Regarding the $p_d$ of $V_N$ at (0, 50), ultra-high $P_I$ of 50 MPa would increase the proportion of droplets near 0 m/s $V_N$. The second peak of the $p_d$ curves for gasoline are slightly higher compared to ethanol under the same $P_I$.

(2) As $t$ progresses, average $V_N$ demonstrates a clear reduction, and the occurrence of an initial reduction can be advanced to 0.7 ms ASOI under $P_I$ = 50 MPa.

(3) Regarding the average $V_T$ at 50 mm of jet downstream, gasoline is about 5.4% greater than ethanol under the same $P_I$, which would promote the horizontal development of the spray, increasing the homogeneity of the air–fuel mixture.

(4) By increasing from 10 MPa to 50 MPa, $p_d$ of large droplets over 20 μm shows a significant decrease, suggesting that the secondary atomisation process is effectively expedited under ultra-high injection pressures.

(5) In comparison to ethanol, the $p_d$ curve's peak of $D_d$ at (0, 50) for gasoline is 1.3 percentage points higher on average under the same $P_I$. Compared to $P_I$ = 10 MPa, $p_d$ of the "$We < 100$" region for both gasoline and ethanol has a moderate reduction under $P_I$ = 50 MPa, while $p_d$ of the regions of "$100 \leq We < 1000$" and "$We \geq 1000$" increases by 23%.

(6) For the variations of $D_{SMD}$ along the horizontal positions, gasoline spray shows a relatively sharp decline on the jet edge (−16, 50) or (16, 50) owing to higher $We$ and vapour density.

(7) Along the vertical direction of the jet, a gradual increase in $D_{SMD}$ can be found for both gasoline and ethanol spray. Under $P_I$ = 50 MPa, the increment in $D_{SMD}$ between (0, 50) and (0, 70) can be up to 3.3 μm, which is more pronounced than that under relatively low $P_I$ conditions.

**Author Contributions:** X.L.: Conceptualization, Methodology, Formal analysis, Investigation, Visualization, Writing—original draft. X.Z.: Conceptualization. T.Z.: Visualization, Writing—reviewing and editing. C.J.: Visualization. P.N.: Formal analysis. W.L.: Formal analysis. Y.P.: Methodology, Project administration, Funding acquisition. Z.P.: Conceptualization, Writing—reviewing and editing. R.M.: Writing—reviewing and editing. All authors have read and agreed to the published version of the manuscript.

**Funding:** This work is supported by the National Engineering Laboratory for Mobile Source Emission Control Technology (No. NELMS2017C01), and the National Key R&D Program of China (No. 2017YFE0116100).

**Institutional Review Board Statement:** Not applicable.

**Informed Consent Statement:** Not applicable.

**Data Availability Statement:** Data will be made available on request.

**Conflicts of Interest:** The authors declare no conflicts of interest.

## Nomenclature

| | |
|---|---|
| ASOI | After Start of fuel Injection |
| BEV | Battery Electric Vehicle |
| DI | Direct Injection |
| ECU | Electronic Control Unit |
| FCEV | Fuel Cell Electric Vehicle |
| GDI | Gasoline Direct Injection |
| HEV | Hybrid Electric Vehicle |
| ICE | Internal Combustion Engine |
| OFC | Oxy-Fuel Combustion |
| PDPA | Phase Doppler Particles Analyser |
| PM | Particulate Matter |
| SAE | Society of Automotive Engineers |
| SI | Spark Ignition |
| $D_d$ | Droplet diameter |
| $D_{SMD}$ | Sauter mean diameter of droplets |
| $P_I$ | Fuel injection pressure |
| $p_d$ | Probability |
| $Re$ | Reynolds number |
| $t$ | Time after start of fuel injection |
| $V_N$ | Normal component of droplet velocity |
| $V_T$ | Tangential component of droplet velocity |
| $We$ | Weber number |

## References

1. Daellenbach, K.R.; Uzu, G.; Jiang, J.; Cassagnes, L.-E.; Leni, Z.; Vlachou, A.; Stefenelli, G.; Canonaco, F.; Weber, S.; Segers, A.; et al. Sources of particulate-matter air pollution and its oxidative potential in Europe. *Nature* **2020**, *587*, 414–419. [CrossRef] [PubMed]
2. Huang, Y.; Lei, C.; Liu, C.-H.; Perez, P.; Forehead, H.; Kong, S.; Zhou, J.L. A review of strategies for mitigating roadside air pollution in urban street canyons. *Environ. Pollut.* **2021**, *280*, 116971. [CrossRef] [PubMed]
3. Li, X.; Li, D.; Liu, J.; Ajmal, T.; Aitouche, A.; Mobasheri, R.; Rybdylova, O.; Pei, Y.; Peng, Z. Exploring the potential benefits of Ethanol Direct Injection (EDI) timing and pressure on particulate emission characteristics in a Dual-Fuel Spark Ignition (DFSI) engine. *J. Clean. Prod.* **2022**, *357*, 131938. [CrossRef]
4. Wong, P.K.; Ghadikolaei, M.A.; Chen, S.H.; Fadairo, A.A.; Ng, K.W.; Lee, S.M.Y.; Xu, J.C.; Lian, Z.D.; Li, S.; Wong, H.C.; et al. Physicochemical and cell toxicity properties of particulate matter (PM) from a diesel vehicle fueled with diesel, spent coffee ground biodiesel, and ethanol. *Sci. Total Environ.* **2022**, *824*, 153873. [CrossRef] [PubMed]

5. Chen, H.; Su, X.; Sun, F.; He, J.; Chen, Z.; Zhang, P.; Xu, H. Investigation on combustion and emission characteristics of a CRDI engine fueled with diesel cyclopentanol blends and verification through on-road real-time test. *Fuel Process. Technol.* **2022**, *234*, 107321. [CrossRef]
6. Abdul-Manan, A.F.; Gordillo Zavaleta, V.; Agarwal, A.K.; Kalghatgi, G.; Amer, A.A. Electrifying passenger road transport in India requires near-term electricity grid decarbonisation. *Nat. Commun.* **2022**, *13*, 2095. [CrossRef]
7. Olabi, A.; Abdelkareem, M.A.; Wilberforce, T.; Alkhalidi, A.; Salameh, T.; Abo-Khalil, A.G.; Hassan, M.M.; Sayed, E.T. Battery electric vehicles: Progress, power electronic converters, strength (S), weakness (W), opportunity (O), and threats (T). *Int. J. Thermofluids* **2022**, *16*, 100212. [CrossRef]
8. Guo, J.; Jiang, Y.; Yu, Y.; Liu, W. A novel energy consumption prediction model with combination of road information and driving style of BEVs. *Sustain. Energy Technol. Assess.* **2020**, *42*, 100826. [CrossRef]
9. Jin, D.; Jiao, K. Charging infrastructure intellectualization and future of different automotive powertrains. *Joule* **2020**, *4*, 1634–1636. [CrossRef]
10. Yap, K.Y.; Chin, H.H.; Klemeš, J.J. Solar Energy-Powered Battery Electric Vehicle charging stations: Current development and future prospect review. *Renew. Sustain. Energy Rev.* **2022**, *169*, 112862. [CrossRef]
11. Niri, A.J.; Poelzer, G.A.; Zhang, S.E.; Rosenkranz, J.; Pettersson, M.; Ghorbani, Y. Sustainability challenges throughout the electric vehicle battery value chain. *Renew. Sustain. Energy Rev.* **2024**, *191*, 114176. [CrossRef]
12. Liu, Y.; Tu, Z.; Chan, S.H. Applications of ejectors in proton exchange membrane fuel cells: A review. *Fuel Process. Technol.* **2021**, *214*, 106683. [CrossRef]
13. İnci, M.; Büyük, M.; Demir, M.H.; İlbey, G. A review and research on fuel cell electric vehicles: Topologies, power electronic converters, energy management methods, technical challenges, marketing and future aspects. *Renew. Sustain. Energy Rev.* **2021**, *137*, 110648. [CrossRef]
14. Huang, H.; Liu, M.; Li, X.; Guo, X.; Wang, T.; Li, S.; Lei, H. Numerical simulation and visualization study of a new tapered-slope serpentine flow field in proton exchange membrane fuel cell. *Energy* **2022**, *246*, 123406. [CrossRef]
15. Huang, H.; Li, X.; Li, S.; Guo, X.; Liu, M.; Wang, T.; Lei, H. Evaluating the effect of refined flow channels in a developed biomimetic flow field on PEMFC performance. *Energy* **2023**, *266*, 126442. [CrossRef]
16. Sahin, H. Hydrogen refueling of a fuel cell electric vehicle. *Int. J. Hydrogen Energy* **2024**, *75*, 604–612. [CrossRef]
17. Kalghatgi, G.; Levinsky, H.; Colket, M. Future transportation fuels. *Prog. Energy Combust. Sci.* **2018**, *69*, 103–105. [CrossRef]
18. Qi, Y.; Liu, W.; Liu, S.; Wang, W.; Peng, Y.; Wang, Z. A review on ammonia-hydrogen fueled internal combustion engines. *eTransportation* **2023**, *18*, 100288. [CrossRef]
19. Liu, L.; Tan, F.; Wu, Z.; Wang, Y. Combining genetic algorithm and deep learning to optimize a chemical kinetic mechanism of ammonia under high pressure. *Fuel* **2024**, *360*, 130508. [CrossRef]
20. Tang, Y.; Xing, K.; Huang, H.; Tu, Z.; Wang, Y.; Guo, X. Simulation study of N2/Ar dilution gas to improve thermal efficiency and reduce NOX emissions in hydrogen engines. *Int. J. Hydrog. Energy* **2024**, *49*, 636–651. [CrossRef]
21. Gao, J.; Wang, X.; Song, P.; Tian, G.; Ma, C. Review of the backfire occurrences and control strategies for port hydrogen injection internal combustion engines. *Fuel* **2022**, *307*, 121553. [CrossRef]
22. Valera-Medina, A.; Xiao, H.; Owen-Jones, M.; David, W.I.; Bowen, P.J. Ammonia for power. *Prog. Energy Combust. Sci.* **2018**, *69*, 63–102. [CrossRef]
23. Valera-Medina, A.; Amer-Hatem, F.; Azad, A.K.; Dedoussi, I.C.; de Joannon, M.; Fernandes, R.X.; Glarborg, P.; Hashemi, H.; He, X.; Mashruk, S.; et al. Review on ammonia as a potential fuel: From synthesis to economics. *Energy Fuels* **2021**, *35*, 6964–7029. [CrossRef]
24. Wang, H.; Wang, B.; Yang, C.; Hu, D.; Duan, B.; Wang, Y. Study on dual injection strategy of diesel ignition ammonia/hydrogen mixture fuel engine. *Fuel* **2023**, *348*, 128526. [CrossRef]
25. Li, X.; Pei, Y.; Peng, Z.; Ajmal, T.; Rana, K.-J.; Aitouche, A.; Mobasheri, R. Numerical study on the effects of intake charge on oxy-fuel combustion in a dual-injection spark ignition engine at economical oxygen-fuel ratios. *Int. J. Engine Res.* **2022**, *23*, 1602–1616. [CrossRef]
26. Serrano, J.R.; Arnau, F.J.; García-Cuevas, L.M.; Gutiérrez, F.A. Coupling an oxygen generation cycle with an oxy-fuel combustion spark ignition engine for zero NOx emissions and carbon capture: A feasibility study. *Energy Convers. Manag.* **2023**, *284*, 116973. [CrossRef]
27. Kang, Z.; Bai, Y.; Feng, S.; Wu, J.; Wu, Z. Effect of direct water injection timing on cycle performance and emissions characteristics within a CI-ICRC engine. *Alex. Eng. J.* **2023**, *72*, 135–145. [CrossRef]
28. Wu, Z.; Fu, L.; Gao, Y.; Yu, X.; Deng, J.; Li, L. Thermal efficiency boundary analysis of an internal combustion Rankine cycle engine. *Energy* **2016**, *94*, 38–49. [CrossRef]
29. Serrano, J.; Martín, J.; Gomez-Soriano, J.; Raggi, R. Theoretical and experimental evaluation of the spark-ignition premixed oxy-fuel combustion concept for future CO2 captive powerplants. *Energy Convers. Manag.* **2021**, *244*, 114498. [CrossRef]
30. Li, X.; Peng, Z.; Pei, Y.; Ajmal, T.; Rana, K.J.; Aitouche, A.; Mobasheri, R. Oxy-fuel combustion for carbon capture and storage in internal combustion engines–A review. *Int. J. Energy Res.* **2022**, *46*, 505–522. [CrossRef]

31. Yue, Z.; Wang, X.; Liu, H.; Li, B.; Yao, M. Exploring the application of oxy-fuel combustion to methanol spark ignition engines. *Appl. Energy* **2024**, *367*, 123449. [CrossRef]
32. Reitz, R.D.; Ogawa, H.; Payri, R.; Fansler, T.; Kokjohn, S.; Moriyoshi, Y.; Agarwal, A.; Arcoumanis, D.; Assanis, D.; Bae, C.; et al. IJER editorial: The future of the internal combustion engine. *Int. J. Engine Res.* **2020**, *21*, 3–10. [CrossRef]
33. Duan, X.; Deng, B.; Liu, Y.; Li, Y.; Liu, J. Experimental study the impacts of the key operating and design parameters on the cycle-to-cycle variations of the natural gas SI engine. *Fuel* **2021**, *290*, 119976. [CrossRef]
34. Chen, Z.; Zhao, P.; Wang, T.; He, H.; Chen, H.; Zhang, P.; Li, Y.; Geng, L.; Qi, D. Visualization study the cross spray and combustion characteristics of diesel and methanol in a constant volume combustion chamber at cold and flare flash boiling regions. *Energy* **2024**, *301*, 131654. [CrossRef]
35. Huang, Y.; Surawski, N.C.; Zhuang, Y.; Zhou, J.L.; Hong, G. Dual injection: An effective and efficient technology to use renewable fuels in spark ignition engines. *Renew. Sustain. Energy Rev.* **2021**, *143*, 110921. [CrossRef]
36. Li, D.; Yu, X.; Du, Y.; Xu, M.; Li, Y.; Shang, Z.; Zhao, Z. Study on combustion and emissions of a hydrous ethanol/gasoline dual fuel engine with combined injection. *Fuel* **2022**, *309*, 122004. [CrossRef]
37. Feng, H.; Lai, K.; Zheng, Z.; Lin, S.; Wu, X.; Tang, Q. Effects of methanol direct injection and high compression ratio on improving the performances of a spark-ignition passenger car engine. *Fuel* **2024**, *357*, 130052. [CrossRef]
38. Lee, Z.; Kim, T.; Park, S.; Park, S. Review on spray, combustion, and emission characteristics of recent developed direct-injection spark ignition (DISI) engine system with multi-hole type injector. *Fuel* **2020**, *259*, 116209. [CrossRef]
39. Maricq, M.M. Engine, aftertreatment, fuel quality and non-tailpipe achievements to lower gasoline vehicle PM emissions: Literature review and future prospects. *Sci. Total Environ.* **2023**, *866*, 161225. [CrossRef]
40. Lee, S.; Park, S. Experimental study on spray break-up and atomization processes from GDI injector using high injection pressure up to 30 MPa. *Int. J. Heat Fluid Flow* **2014**, *45*, 14–22. [CrossRef]
41. Medina, M.; Alzahrani, F.; Fatouraie, M.; Wooldridge, M.S.; Sick, V. Mechanisms of fuel injector tip wetting and tip drying based on experimental measurements of engine-out particulate emissions from gasoline direct-injection engines. *Int. J. Engine Res.* **2021**, *22*, 2035–2053. [CrossRef]
42. Hoffmann, G.; Befrui, B.; Berndorfer, A.; Piock, W.F.; Varble, D.L. Fuel system pressure increase for enhanced performance of GDi multi-hole injection systems. *SAE Int. J. Engines* **2014**, *7*, 519–527. [CrossRef]
43. Song, J.; Lee, Z.; Song, J.; Park, S. Effects of injection strategy and coolant temperature on hydrocarbon and particulate emissions from a gasoline direct injection engine with high pressure injection up to 50 MPa. *Energy* **2018**, *164*, 512–522. [CrossRef]
44. Lee, Z.; Park, S. Particulate and gaseous emissions from a direct-injection spark ignition engine fueled with bioethanol and gasoline blends at ultra-high injection pressure. *Renew. Energy* **2020**, *149*, 80–90. [CrossRef]
45. Li, X.; Li, D.; Liu, J.; Ajmal, T.; Aitouche, A.; Mobasheri, R.; Rybdylova, O.; Pei, Y.; Peng, Z. Comparative Study on the macroscopic characteristics of gasoline and ethanol spray from a GDI injector under injection pressures of 10 and 60 Mpa. *ACS Omega* **2022**, *7*, 8864–8873. [CrossRef] [PubMed]
46. Li, X.; Zhang, X.; Ni, P.; Weerasinghe, R.; Pei, Y.; Peng, Z. Insights into the spray impingement process from a gasoline direct injection fuel system fuelled with gasoline and ethanol. *J. Energy Inst.* **2023**, *110*, 101331. [CrossRef]
47. Luo, H.; Nishida, K.; Ogata, Y.; Zhang, W. Microscopic characteristics of near-nozzle spray at the initial and end stages. *Fuel* **2021**, *283*, 118953. [CrossRef]
48. Zhang, G.; Luo, H.; Kita, K.; Ogata, Y.; Nishida, K. Statistical variation analysis of fuel spray characteristics under cross-flow conditions. *Fuel* **2022**, *307*, 121887. [CrossRef]
49. Zhang, M.; Ge, Y.; Wang, X.; Xu, H.; Tan, J.; Hao, L. Effects of ethanol and aromatic compositions on regulated and unregulated emissions of E10-fuelled China-6 compliant gasoline direct injection vehicles. *Renew. Energy* **2021**, *176*, 322–333. [CrossRef]
50. Zhang, Z.; Li, J.; Tian, J.; Dong, R.; Zou, Z.; Gao, S.; Tan, D. Performance, combustion and emission characteristics investigations on a diesel engine fueled with diesel/ethanol/n-butanol blends. *Energy* **2022**, *249*, 123733. [CrossRef]
51. da Costa, R.B.R.; Roque, L.F.A.; De Souza, T.A.Z.; Coronado, C.J.R.; Pinto, G.M.; Cintra, A.J.A.; Raats, O.O.; Oliveira, B.M.; Frez, G.V.; Da Silva, M.H. Experimental assessment of renewable diesel fuels (HVO/Farnesane) and bioethanol on dual-fuel mode. *Energy Convers. Manag.* **2022**, *258*, 115554. [CrossRef]
52. Ooi, J.B.; Kau, C.C.; Manoharan, D.N.; Wang, X.; Tran, M.V.; Hung, Y.M. Effects of multi-walled carbon nanotubes on the combustion, performance, and emission characteristics of a single-cylinder diesel engine fueled with palm-oil biodiesel-diesel blend. *Energy* **2023**, *281*, 128350. [CrossRef]
53. Li, X.; Pei, Y.; Ajmal, T.; Rana, K.J.; Aitouche, A.; Mobasheri, R.; Peng, Z. Numerical investigation on implementing Oxy-Fuel Combustion (OFC) in an ethanol-gasoline Dual-Fuel Spark Ignition (DFSI) engine. *Fuel* **2021**, *302*, 121162. [CrossRef]
54. Harrington, D.L.; Gandhi, A.H.; Markle, L.E.; Parrish, S.E.; Shakal, J.S.; Sayar, H.; Cummings, S.D.; Kramer, J.L. Gasoline fuel injector spray measurement and characterization–a new SAE J2715 recommended practice. *SAE Int. J. Fuels Lubr.* **2009**, *1*, 534–548.

55. Arcoumanis, C.; Gavaises, M.; French, B. Effect of fuel injection processes on the structure of diesel sprays. *SAE Trans.* **1997**, *106*, 1025–1064.
56. Lee, S.; Oh, Y.; Park, S. Characterization of the spray atomization process of a multi-hole gasoline direct injector based on measurements using a phase Doppler particle analyser. *Proc. Inst. Mech. Eng. Part D J. Automob. Eng.* **2013**, *227*, 951–965. [CrossRef]

**Disclaimer/Publisher's Note:** The statements, opinions and data contained in all publications are solely those of the individual author(s) and contributor(s) and not of MDPI and/or the editor(s). MDPI and/or the editor(s) disclaim responsibility for any injury to people or property resulting from any ideas, methods, instructions or products referred to in the content.